Dynamics of high-energy proton beam acceleration and focusing from hemisphere-cone targets by high-intensity lasers

B. Qiao, M. E. Foord, M. S. Wei, R. B. Stephens, M. H. Key, H. McLean, P. K. Patel, and F. N. Beg

Phys. Rev. E **87**, 013108 — Published 25 January 2013

DOI: 10.1103/PhysRevE.87.013108

Dynamics of high-energy proton beam acceleration and focusing from hemisphere-cone target irradiated by high-intensity lasers

B. Qiao,[1,*] M. E. Foord,[2] M. S. Wei,[3] R. B. Stephens,[3]
M. H. Key,[2] H. McLean,[2] P. K. Patel,[2] and F. N. Beg[1,†]

[1]*Center for Energy Research, University of California San Diego, La Jolla, California 92093 USA*

[2]*Lawrence Livermore National Laboratory, Livermore, California 94511, USA*

[3]*General Atomics, San Diego, California 92121, USA*

Abstract

Acceleration and focusing of high-energy proton beams from fast-ignition (FI) related, hemisphere-cone assembled target have been numerically studied by hybrid particle-in-cell simulations, and compared with those from the planar-foil and open-hemisphere targets. The whole physical process including the laser-plasma interaction has been self-consistently modeled for 15 picoseconds at which time protons reach the asymptotic motions. It is found that the achievable focus of proton beams is limited by the thermal pressure gradients in the co-moving hot electrons, which induces a transverse defocusing electric field that bends proton trajectories near the axis. For the advanced hemisphere-cone target, the flow of hot electrons along the cone wall induces a local transverse focusing sheath field, resulting in a clear enhancement in proton focusing; however, it leads to a significant loss of longitudinal sheath potential reducing the total conversion efficiency from laser to protons.

PACS numbers: 52.38.Kd, 52.57.Kk, 52.65.Rr, 52.50.Jm

*Electronic address: bqiao@ucsd.edu

†Electronic address: fbeg@ucsd.edu

I. INTRODUCTION

Since the first observations [1] of intense, beam-like emission of >10MeV protons from a solid foil target, many prospective applications of laser-driven proton beams have been proposed. These [2] include isotope production, tumor therapy, ultrafast radiography, and inertial confinement fusion. Among them, the concept of using laser-driven proton beams to ignite a fast ignition (FI) target [3, 4] has aroused great interest. The much larger mass-to-charge ratio of the proton relative to the electron creates a more stable particle beam as ignitor that is much less sensitive to the strong self-generated E and B fields induced during their energy transport in dense plasmas. Furthermore, a characteristic of proton acceleration from a laser-irradiated foil, generally attributed to the target normal sheath acceleration (TNSA) mechanism [5, 6], allows using the curved full/partial hemisphere targets to focus the proton beam from a relatively large target to a small spot size (10s of microns) with an extremely high energy density [7–10]. This eases requirements on laser focus and intensity, and allows for the design for both the optimum particle energy and the requisite particle beam density for FI.

In TNSA, protons and electrons constitute a quasi-neutral plasma jet undergoing thermal expansion into vacuum driven by the hot electron pressure. For the proton FI scheme, the source target must be shielded from intense soft X-ray radiation generated around the imploding target during the compression stage. The partial hemisphere target is therefore protected by a surrounding cone structure (hereafter we refer to this assembled target as a "hemisphere-cone" target) [4], similar to the one proposed for electron FI [11, 12]. Such a surrounding cone structure would significantly affect the acceleration and focusing dynamics of proton beams. Recent experiments on Trident laser [13] found that the hemisphere-cone targets produce significantly smaller focal spot diameters of proton beams relative to the open-hemisphere targets. The particle-in-cell simulations [14], which model the proton acceleration process by injecting an assumed laser-heated electron source, show that the electric fields in the plasma and on the cone structure wall play an important role in determining the focusing characteristics of the beam. However, a self-consistent and systematical study that includes the role that hot electrons produced in the laser-plasma interaction (LPI) process play in the dynamics of proton beams for different target geometries has not been carried out. In particular, two important elements need to be self-consistently demonstrated

in the advanced hemisphere-cone target: 1) an effective focusing of protons, 2) a sufficient conversion efficiency of energy from laser to protons, comparing to the planar-foil and open-hemisphere targets. A large scale proton FI design requires a high power laser (energy 100s kJ and pulse duration 10 ps) to irradiate on the hemisphere-cone target, producing a focused proton beam with energy 20 kJ, diameter $< 40\mu$m and mean energy of 10 MeV, where the conversion efficiency from laser to protons is above 15%.

In this paper, we carry out a self-consistent theoretical and numerical study for proton beam acceleration and focusing from the advanced FI-related hemisphere-cone targets. The results are characterized through comparisons with both the planar-foil and open-hemisphere target geometries. The massively-parallel implicit particle-in-cell (PIC) code, Large-Scale-Plasma (LSP) [15, 16], with the self-consistent LPI package is used for integrated modeling of the complete physical process starting with hot electron production in the LPI, proceeding through proton beam's initial strong transient acceleration and thermal expansion for 15 picoseconds, which is the time necessary for protons to reach asymptotic velocities. The simulation results are explained by simple fluid theory.

The paper is organized as follows: in Sec. II, we describe the integrated PIC simulation setup and show the hot electron production dynamics for respectively planar-foil, open-hemisphere and advanced hemisphere-cone targets; in Sec. III, detailed analyses and comparisons of proton acceleration and focusing dynamics for the three different target geometries are given; Sec. IV gives the conversion efficiency analysis for the different targets; a summary and discussion are given in Sec. V.

II. INTEGRATED PIC SIMULATION SETUP AND HOT ELECTRON PRODUCTION

The simulations of proton acceleration and focusing from different target geometries are performed using the implicit relativistic electromagnetic PIC code LSP [15, 16]. The benefits of the fully implicit algorithm treatment are that the usual charged particle limitations on the time step, namely the need to resolve the cyclotron and plasma frequencies, are relaxed although both frequencies cannot be under resolved at the same time and position. Including an inertial fluid electron algorithm further improves energy conservation for long simulation times. These features of LSP allow us to model the whole process of proton

beam acceleration, focusing and thermal expansion for 15 ps, which is the time necessary for protons to reach their asymptotic velocities. The roles of the laser-heated electrons in determining proton conversion efficiency and focus have not been previously considered [13, 14].

The simulations are conducted in two spatial dimensions (2D), in a system domain of 400μm transversely along x-direction and 700μm longitudinally along the z-direction, which is composed of 3200×4000 cells (nonuniform grids with the smallest cell size 0.1μm). The zero potential, perfect conducting boundary condition is used on all sides apart from the left outlet boundary from which the laser propagates into the simulation box. These boundaries are perfect absorbers of impacting particles, preventing the target and the simulation area from charging up numerically for such a long simulation. Collisions are also included in the simulation based on the Spitzer collision frequencies, where the hot electron scattering, dragging, and slowing-down rates have been calculated. A 1μm wavelength laser with peak intensity $I_0 = 4 \times 10^{19}\mathrm{Wcm}^{-2}$, Gaussian distribution $\exp[-(x/r_0)^2]$ of $r_0 = 45\mu$m enters from the left boundary $z = -50\mu$m and irradiates the target located at $z = 0$. The laser pulse has a trapezoidal temporal profile of duration 600fs, consisting of a plateau of 500fs and rising and falling times of 50fs each. Three geometries of carbon targets are modeled, shown in Fig. 1, respectively of planar-foil, open-hemisphere and advanced hemisphere-cone targets, where the ion charge states of C^{4+}, mass density of 2.7g/cc and thickness of 10μm are assumed. The partial hemisphere targets have a radius of curvature 300μm and a chord length 300μm. The cone structure for the hemisphere-cone target is assumed to be composed of Al with charge state 10+. The preplasma profile for the three cases is assumed to be the same exponential $\exp(-z/L)$ with scale length $L = 4\mu$m. A hydrocarbon contamination layer of thickness 50nm is appended to the rear surfaces of all the targets and the cone wall surfaces. In the following, we analyze and compare proton acceleration and focusing dynamics for these three representative targets.

For targets with thickness large enough to prevent the laser from punching through, the ion acceleration takes place in the purely TNSA regime. The laser interacts mostly with the preplasma. As shown in Fig. 2, the laser fields propagate and penetrate to the relativistic critical surface γn_c ($\sim 5.7 \times 10^{21}\mathrm{cm}^{-3}$ roughly at $z = -21\mu$m) and decay afterwards quickly in a distance of the skin depth. Hot electrons are generated in this preplasma region by LPI and quickly they move forward into the solid dense target. The time-integrated energy

spectra of hot electrons propagating through a diagnostic plane at $z = -10\mu$m, 10μm behind the critical surface, are shown in Fig. 3(j). It shows that the hot electron sources obtained from LPI are similar for the three cases though the target geometries are different. The energy spectra have the similar slope temperature of $T_e \simeq 2.1$MeV, consistent with the ponderomotive scaling [17] on laser intensity I for $I = 4 \times 10^{19}\mathrm{W/cm}^2$.

Despite a large current of these hot electrons, they still propagate nearly ballistically in the thin low-Z carbon target, where the charge neutralization is excellent until reaching the rear surface where the ratio of the space charge to relativistic energy is large. Figures 3(a), 3(d) and 3(g) show the hot electron density distributions at time $t = 600$fs for different target geometries when the laser pulse is just over. It can be seen that only a small minority of the hot electrons at the high-energy tail [up to 28MeV in Fig. 3(j)] can escape far away into vacuum. The escape of these electrons set up a strong sheath potential trapping the majority of hot electrons at the target rear side forming a hot electron "cloud". The trapped electrons reflect from the potential, retain their transverse motion and spread across the target. During the 600fs pulse duration, the electrons can traverse the thin target (10μm thickness for either hemisphere or planar foil) many times, finally filling a vacuum space near the target back surface transversely up to 150μm in x-direction. The electron cloud extends into the vacuum with $10^{18}\mathrm{cm}^{-3}$ about 10 μm outside the original boundary over much of the surface but the density falls off rapidly beyond, because the hot electron Debye length $\lambda_{D,h} = (T_h/4\pi n_h e^2)^{1/2}$ is about 10.5μm if $T_h = 2$MeV as was calculated above.

III. PROTON ACCELERATION AND FOCUSING IN DIFFERENT TARGET GEOMETRIES

The hot electron cloud at the rear side of the target results in a strong space charge potential for proton acceleration and thermal expansion. The electric field driven by the hot electron pressure can be estimated as [13, 18] $\mathbf{E} \simeq -(\gamma_e/en_e)\nabla\Pi_e$, where n_e and T_e are respectively the local density and temperature of the hot electrons, and $\Pi_e = n_e T_e$ is the hot electron thermal pressure. The electric field has both transverse and longitudinal

components as

$$E_x \simeq -\frac{\gamma_e}{en_e}\frac{\partial(n_e T_e)}{\partial x}, \tag{1}$$

$$E_z \simeq -\frac{\gamma_e}{en_e}\frac{\partial(n_e T_e)}{\partial z}, \tag{2}$$

which play roles in respectively focusing and accelerating of protons.

Initially a sharp sheath field is formed at the target rear surface before protons start to move. The accelerating force on the outmost protons can be approximately expressed as [5] $m_i d\mathbf{v_i}/dt = (\gamma_e n_e/n_i)(T_e/L_n)\hat{e}_{L_n}$, where $\mathbf{L_n} = L_n\hat{e}_{L_n} = [1/n_e(\partial n_e/\partial x\hat{e}_x + \partial n_e/\partial y\hat{e}_y + \partial n_e/\partial z\hat{e}_z)]^{-1}$ is the local plasma scale length in the different directions. Because the smallest plasma scale length direction $\hat{e}_{L_n}$ initially is normal to the target surface direction, where $L_n \to 0$, therefore the sheath electric field and the proton acceleration is always dominantly along the direction normal to the target rear surface at initial transient time. For the curved hemisphere targets, the electric field has stronger transverse component E_x, shown in [Figs. 4(d) and 4(g)], leading in principle to geometrical focusing of protons initially as expected for TNSA.

However, at later time after protons are accelerated into vacuum, they together with the co-moving hot electrons form a quasi-neutral plasma jet undergoing thermal expansion driven by the local hot electron pressure obeying Eqs. (1) and (2). During this thermal expansion stage, proton acceleration and foucsing behaviors heavily depend on the hot electron dyanmics, which are significantly influenced by the target geometries, in particular, by the surrounding cone structure.

Figure 3 shows the hot electron density distributions at $t = 0.6$, 1.0 and 1.4ps for the three targets. On the one hand, we see that a major fraction of hot electrons co-move with protons and transfer their energies to protons by cooling down themselves. On the other hand, another significant fraction of hot electrons are diffused away from the laser focus along the target surface (to the surrounding cone structure for the hemisphere-cone target case). In particular, the longitudinal sheath electric field E_z together with the magnetic field B_y, induced by the density gradient between the target rear surface and the vacuum, confine a number of hot electrons to flow along the target rear surface, forming a surface current similar to those in the electron FI scheme [19]. This surface current can be maintained along the cone wall for the hemisphere-cone target, as seen in Figs. 3(h), 3(i), 4(h) and 4(i).

The above complex hot electron dynamics leads to different proton focusing dynamics depending on the target geometries. For the planar-foil target, the surface current mentioned above disappears rapidly after protons expand into vacuum, and apparently the hot electron thermal pressure in the plasma is higher close to the laser axis with gradient directed transversely outward due to the finite laser focus. Therefore, according to Eq. (1), the transverse electric field E_x changes its sign quickly at $t = 1.4$ps to be transversely outward (defocusing), see Fig. 4(c), resulting in spreading of the proton beam. For the open-hemisphere target, the surface current can be maintained for a longer distance in the z-direction along the curved surface, and the transverse component of the sheath field E_x can be maintained out to $z \approx 100\mu$m [Fig. 4(e)] (E_x also diffuses from the surface into vacuum significantly) for proton focusing. Beyond this, the sign of E_x changes [4(f)] due to the hot electron pressure gradient in the expanding plasma [Eq. (1)], which bends the proton trajectories and limits the achievable focus.

However, for the hemisphere-cone target case, the hot electron flow is guided/continued along the cone wall surface, maintaining the focusing sheath electric field sign up to the cone tip, as shown in Figs. 4(h) and 4(i). This focusing field diffuses inward significantly from the wall surface into the vacuum, therefore a significant enhanced focusing of proton beams is achieved though the hot electron current is only along the wall surface.

Figure 5 plots the proton density maps at respectively $t = 5$, 10 and 15ps for the different target geometries. A clear enhanced focusing of proton beam can be seen with the advanced hemisphere-cone target comparing to the planar-foil and open-hemisphere targets due to the extension of the focusing electric field E_x along the cone wall, which has both smaller focal radius and no spreading at either the edge of the target or the wing parts of the beam. From the transverse profiles of proton densities around the geometrical focal region shown in 5(j), we see the focal radius decreases about 15% from the open-hemisphere to hemisphere-cone target case. This is consistent with our analysis above. Furthermore it also demonstrates the ability of focusing proton beams to the required 40μm size for proton FI by using the advanced hemisphere-cone target.

Trajectories for a group of test particles that originate along the target rear surface at different transverse positions are shown in Figs. 6(a) and 6(c), illustrating the curvature of proton trajectories respectively for the planar-foil and hemisphere-cone targets. For the planar-foil case, after the initial acceleration normal to the rear surface, the test protons

spread out for all energy ranges because of the transverse defocusing electric field [for example, $E_x > 0$ in 6(b) for the test particle with the trajectory in dark blue line (dark grey with the final achieved energy "4.1MeV")] induced by the transverse outward gradients in hot electron thermal pressure, as discussed above. For the hemisphere-cone target, all test protons are accelerated normal to the surface towards the geometrical center (at $z = 300\mu$m) initially. Afterwards the test particles which were initially located close to the cone wall [the red, grey and light blue lines (the upper three trajectory lines) in 6(c)] continue in almost straight line trajectories because the transverse focusing electric field [$E_x < 0$ up to $z = 200\mu$m, see the red (lower) line in 6(d)] is maintained along the cone wall due to the hot electron surface current. However, the other test particles which were initially located in the center close to the z-axis [the dark blue, dark and purple lines (the lower three trajectory lines) in 6(c)] donot continue in straight line trajectories but bend away after the cone tip due to the transverse defocusing field [$E_x > 0$ beyond $z > 200\mu$m, see the dark blue (upper) line in 6(d)], where the hot electron thermal pressure gradient is directed outwards. These self-intersections in particle trajectories further prove that protons cannot be ballistically focused by merely curving the target spherically and the achievable focusing is limited by the hot electron pressure.

Note that in a realistic 3D geometry, if we assume that more hot electrons are produced and propagate through the target, a denser (higher n_e) hot electron cloud may form at the target rear side. Due to the hot electron pressure, greater transverse electric field E_x [Eq. (1)] inside the expanding plasma jet would be induced, bending proton trajectories much harder than the 2D case here. Therefore, for the planar-foil/open-hemisphere target cases, the achievable focus of proton beams is even worse in the 3D case. However, for the hemisphere-cone case, a larger number of hot electrons are produced, which also leads to greater hot electron flow along the cone wall surface and consequently stronger sheath electric field there to focus proton beams. A combination of these two aspects indicates that more significant enhancement of proton focusing due to the surrounding cone structure may be observed in a realistic 3D case than was observed in the current 2D simulations. An exact comparison of this requires further efforts by large-scale full 3D-PIC simulations.

IV. CONVERSION EFFICIENCY ANALYSIS

As mentioned in the introduction, another important element for proton FI is the requirement of conversion efficiency above 15% from petawatt laser energy to proton beams in the energy range of $5 - 18$MeV [20]. In this section, we analyze the influence of target geometries on the conversion efficiency from laser to protons.

From the above discussions, we already learned that the hot electron diffusion and flow along the target surface into the cone structure results in enhanced focusing of proton beams with the advanced hemisphere-cone target. However, this also leads to a factor of more than 4 drop in density of the hot electrons behind the rear surface [see Figs. 3(i) and 3(k)], as compared to the open-hemisphere case [Fig. 3(f)]. These hot electrons contribute to forming the longitudinal sheath field E_z for proton acceleration, obeying Eq. (2). Therefore, the evolutions of E_z depend significantly on the target geometries, as shown in Fig. 7. Initially at $t = 600$fs, we see that the distributions of E_z are normal to the target rear surface [see 7(a), 7(d) and 7(g)] and their magnitudes [the blue (dark grey) lines in 7(j)-7(l)] are the same for three different target geometries. However, at later time $t = 1.0$ps, we can see from Figs. 7(j)-7(l) [the green (light grey) lines] that E_z for the hemisphere-cone target drops down by a factor of about 2 compared to the planar-foil and/or open-hemisphere target cases. Furthermore, the curvature sheath front in Figs. 7(e) and 7(h) corresponds to the leading edge of the proton beam in expansion, whose magnitude decreases with time during expansion because of cooling down of hot electron thermal pressure gradient [Eq. (2)].

The drop of E_z results in lower conversion efficiency and smaller proton maximum energy for the advanced hemisphere-cone target. Figs. 8(a) and 8(b) show respectively the proton energy spectra at $t = 15$ps and the energy conversion from laser to protons with time for the different target geometries. The proton energy spectra have a similar slope temperature of 2.2MeV, close to the hot electron temperature in Fig. 3(j). However, the overall conversion efficiency from laser to protons is about 4.1%, 3.5% and 1.3% for respectively planar-foil, open-hemisphere and hemisphere-cone targets respectively, that is, a factor of more than 2 decrease in the conversion efficiency due to the attached cone structure in the hemisphere-cone target.

The overall comparative low conversion efficiency to protons for the three target geometries here is due to the heating and acceleration of mixed heavier C4+ ion species in the

hydrocarbon contaminant layer (and the target). It is predicted [21] that the carbon ions can gain more than half the total ion beam energy because of their larger mass, limiting the energy available to the protons. Using a hydrogen-rich back surface coating and a careful choice of target material and laser conditions, much higher conversion efficiency can be achievable. For the hemisphere-cone target, the loss of hot electrons into the cone structure can be improved by reducing the connection area between hemisphere and cone structure, for example by using separate insulating thin tabs.

V. SUMMARY AND DISCUSSION

In summary, we have theoretically and numerically investigated the dynamics of high-energy proton beam acceleration and focusing from respectively planar-foil, open-hemisphere, and hemisphere-cone target geometries by intense laser pulses. Self-consistent demonstrations by integrated implicit particle-in-cell simulations of the whole physical process including laser-plasma interaction have been carried out for the first time for 15 picoseconds, at which time protons reach the asymptotic velocities. We find that the achievable focus of proton beams is limited by the thermal pressure gradient in the drive hot electrons, and the proton trajectories bend away near the focal point. For the advanced FI-related hemisphere-cone target, the flow of hot electrons along the cone wall induces a local transverse focusing sheath electric field, resulting in significantly smaller focal spot diameters relative to either the planar-foil or open-hemisphere targets. However, this diffusion of electrons also leads to loss of the longitudinal sheath potential for proton acceleration, reducing the total conversion efficiency from laser to protons.

These results are of great interest for proton fast ignition point design [4], which requires a high-energy proton beam with intense current of 15-20 kJ and focused diameter of $20-40\mu$m. Increasing the spatial uniformity of the laser is predicted to significantly improve the focusing characteristics of the beam, since the gradient of hot electron pressure in Eq. (1) would be reduced. The proton energy is limited by diffusion of hot-electrons away from the accelerating surface, and the achievable focus is limited by hot electron pressure in the radially converging proton beam. These effects of the hot electron containment (or lack thereof) had not been recognized in previous studies [8–10]. We expect that with longer pulse duration (up to 10 picoseconds) relevant to fast ignition, these effects of electron motion will

be even more significant. The diffusion of hot electrons into the cone structure is responsible for generating the focusing fields on the wall, which, however, is at the expense of reducing the accelerating fields leading to reduced conversion efficiency. This indicates that a proper target design, for example, partially isolating the targets from the cone structure by using separate insulating tabs instead of fully brimmed connection, is needed to achieve a balance. Furthermore, the ability to focus intense proton beams to higher intensities by a proper target design is also critical to the advance of many applications in high-energy density physics, such as isochoric heating of plasma [8], imaging implosion dynamics and magnetic fields [22, 23].

The work was supported by DOE under contract DE-SC0001265. LC computing resources at LLNL are acknowledged. We acknowledge helpful discussions with C. Bellei and C. McGuffey.

---

[1] E. L. Clark *et al.*, Phys. Rev. Lett. **84**, 670 (2000); A. Maksimchuk *et al.*, *ibid.* **84**, 4108 (2000); R. A. Snavely *et al.*, *ibid.* **85**, 2945 (2000).

[2] M. Borghesi et al., Fusion Sci. Technol. **49**, 412 (2006).

[3] M. Roth *et al.*, Phys. Rev. Lett. **86**, 436 (2001).

[4] M.H. Key *et al.*, Fus. Sci. & Technol. **49**, 440 (2006).

[5] S. C. Wilks *et al.*, Phys. Plasmas **8**, 542 (2001).

[6] M. Borghesi *et al.*, Phys. Rev. Lett. **92**, 055003 (2004).

[7] H. Ruhl *et al.*, Plasma Phys. Reports **27**, 363, (2001).

[8] P. K. Patel *et al.*, Phys. Rev. Lett. **91**, 125004 (2003).

[9] R. A. Snavely *et al.*, Inertial Fusion Science and Applications 2003 Proceedings (Pub. American Nuclear Society Inc, p. 349. (2004).

[10] D. T. Offermann *et al.*, Phys. Plasmas **18**, 056713 (2011).

[11] P. A. Norreys *et al.*, Phys. Plasmas **7**, 3721 (2000).

[12] R. Kodama *et al.*, Nature **412**, 798 (2001).

[13] T. Bartal *et al.*, Nature Physics, **8**, 139 (2012).

[14] M. E. Foord *et al.*, Phys. Plasmas **19**, 056702 (2012).

[15] D.R. Welch, D.V. Rose, B.V. Oliver, and R.E. Clark, Nucl. Instrum. and Methods in Phys. Res. A **464**, 134 (2001).

[16] D.R. Welch *et al.*, Phys. Plasmas **13**, 063105 (2006).

[17] S. C. Wilks, W. L. Kruer, M. Tabak, and A. B. Langdon, Phys. Rev. Lett. **69**, 1383 (1992).

[18] C. Bellei *et al.*, Phys. Plasmas **19**, 033109 (2012).

[19] T. Nakamura *et al.*, Phys. Rev. Lett. **93**, 265002 (2004).

[20] D. S. Hey, M. E. Foord, M. H. Key *et al.*, Phys. Plasmas **16**, 123108 (2009).

[21] M. E. Foord, P. K. Patel, A. J. Mackinnon, S. P. Hatchett, M. H. Key, B. Lasinski, R. P. J. Town, M. Tabak, S. C. Wilks, High Energy Density Phys. **3**, 365 (2007).

[22] M. Borghesi, A. Schiavi, D. H. Campbell, M. G. Haines, O. Willi, A. J. Mackinnon, L. A. Gizzi, M. Galimberti, R. J. Clarke and H. Ruhl, Plasma Phys. and Control. Fus., **43**, A267 (2001).

[23] C. K. Li, F. H. Seguin, J. R. Rygg, J. A. Frenje, M. Manuel, R. D. Petrasso, R. Betti, J. Delettrez, J. P. Knauer, F. Marshall, D. D. Meyerhofer, D. Shvarts, V. A. Smalyuk, C. Stoeckl, O. L. Landen, R. P. J. Town, C. A. Back, and J. D. Kilkenny, Phys. Rev. Lett. **100**, 225001 (2008).

FIG. 1: (Color online) Initial electron density maps for different target geometries in LSP simulations, which are respectively (a) planar-foil, (b) open-hemisphere, and (c) hemisphere-cone targets.

FIG. 2: (Color online) The transverse laser electric field E_x in the preplasma region at time (a) $t = 400$ and (b) 600fs for the hemisphere-cone target. Those for the planar-foil and open-hemisphere target cases are similar to here. The blue (dark grey) lines show the corresponding electron density longitudinal profile at the laser-axis. The laser propagates to $z \approx -21\mu$m before it is reflected from the relativistic critical surface $\gamma n_c \sim 5.7 \times 10^{21}\text{cm}^{-3}$.

FIG. 3: (Color online) Hot electron density maps at $t = 0.6$, 1.0 and 1.4ps produced from respectively planar-foil [upper row (a)-(c)], open-hemisphere [middle row (d)-(f)], and FI-relevant advanced hemisphere-cone [bottom row (g)-(i)] targets by laser pulse at intensity $4 \times 10^{19}\text{Wcm}^{-2}$ and duration 600fs. The other parameters are shown in the text. (j) shows the time-integrated energy spectra of hot electrons passing through the diagnostic plane at $z = -10\mu$m, 10μm behind the critical surface. It indicates that the hot electron source produced in the LPI is similar for different target geometries. (k) shows the on-axis longitudinal profiles of hot electron densities at the rear of the target.

FIG. 4: (Color online) The transverse electric field E_x at times $t = 0.6$, 1.0 and 1.4ps for laser interactions with (by row) planar-foil, open-hemisphere, and hemisphere-cone targets, where the laser and target parameters are the same as Fig. 3.

FIG. 5: (Color online) Proton density maps at $t = 5.0$, 10.0 and 15.0ps from respectively planar-foil [upper row (a)-(c)], open-hemisphere [middle row (d)-(f)] and hemisphere-cone [bottom row (g)-(i)], where the laser and target parameters are the same as in Fig. 3. (j) shows the transverse profiles of integrated densities from $z = 250$ to 500μm at $t = 15$ps in (c), (f) and (i) (the region between the dashed lines). It shows a clear enhanced focusing of proton beams with the hemisphere-cone target comparing to the other two geometries.

FIG. 6: (Color online) Trajectories of test particles initially located at different radial positions along the target rear surface for respectively planar-foil (a) and hemisphere-cone (c) targets in the simulation of Fig. 3, where those for the open-hemisphere target case is not plotted here due to its similarity to the hemisphere-cone target. (b) and (d) show respectively the transverse electrostatic fields E_x on the corresponding tracing particles. It shows clearly the curvature of proton trajectories and the bending effect due to the local hot electron thermal pressure gradient.

FIG. 7: (Color online) The longitudinal electric field E_z at times $t = 0.6$, 1.0 and 1.4ps for laser interactions with (by row) planar-foil, open-hemisphere, and hemisphere-cone targets, where the laser and target parameters are the same as in Fig. 3. (j)-(l) show the corresponding longitudinal profiles of E_z on the laser axis.

FIG. 8: (Color online) Proton energy spectra at $t = 15$ps (a) and normalized (by laser energy) energy conversion from laser to protons as a function of time (b) for different target geometries. The black line in (b) shows the laser energy evolution with time and the dashed lines in (b) show the normalized energy conversion from laser to hot electrons diagnosed from the extraction plane in Fig. 3(j). Both (a) and (b) show that the conversion efficiency drops significantly by a factor of more than 2 from open-hemisphere to hemisphere-cone targets.

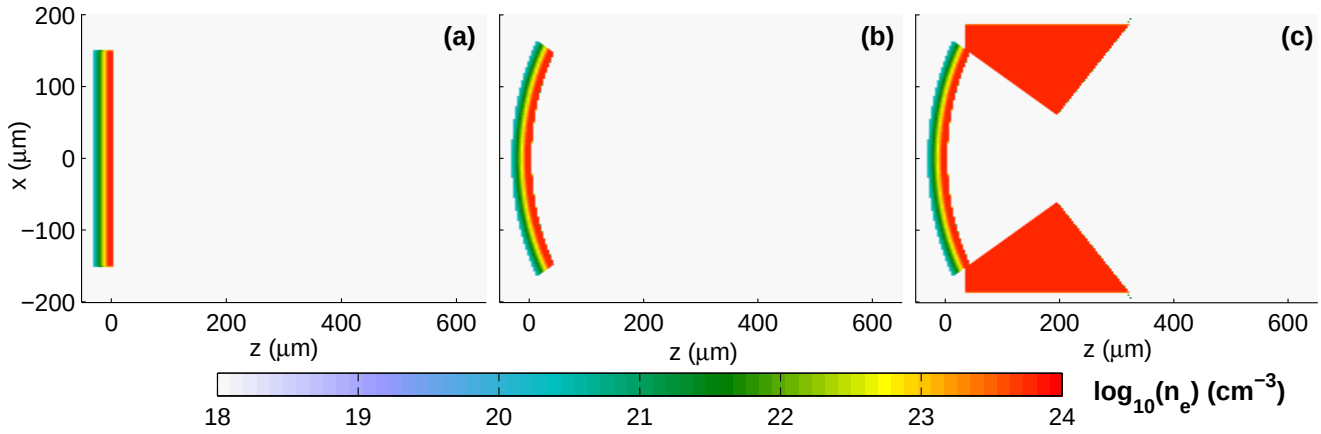

Figure 1 XXXXXXX 10Jan2013

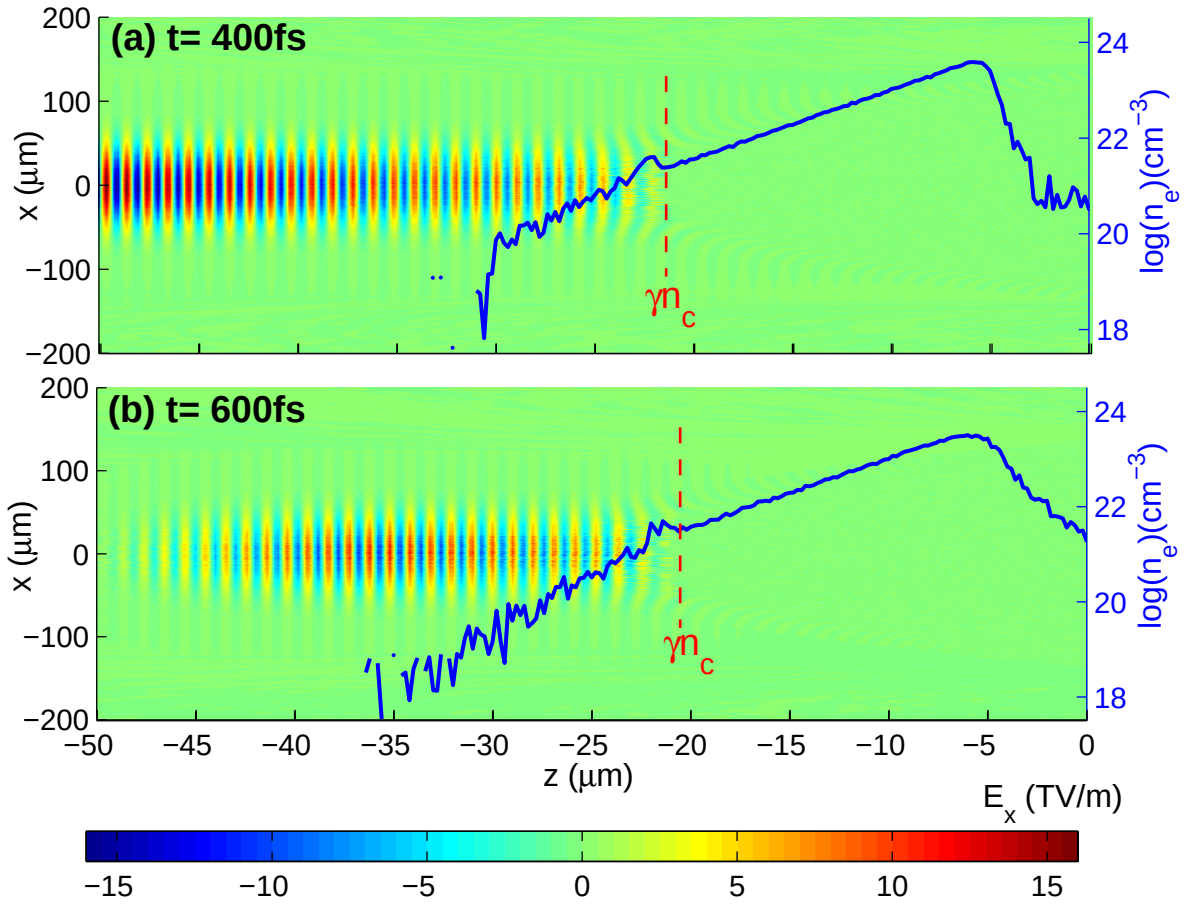

Figure 2 XXXXXXX 10Jan2013

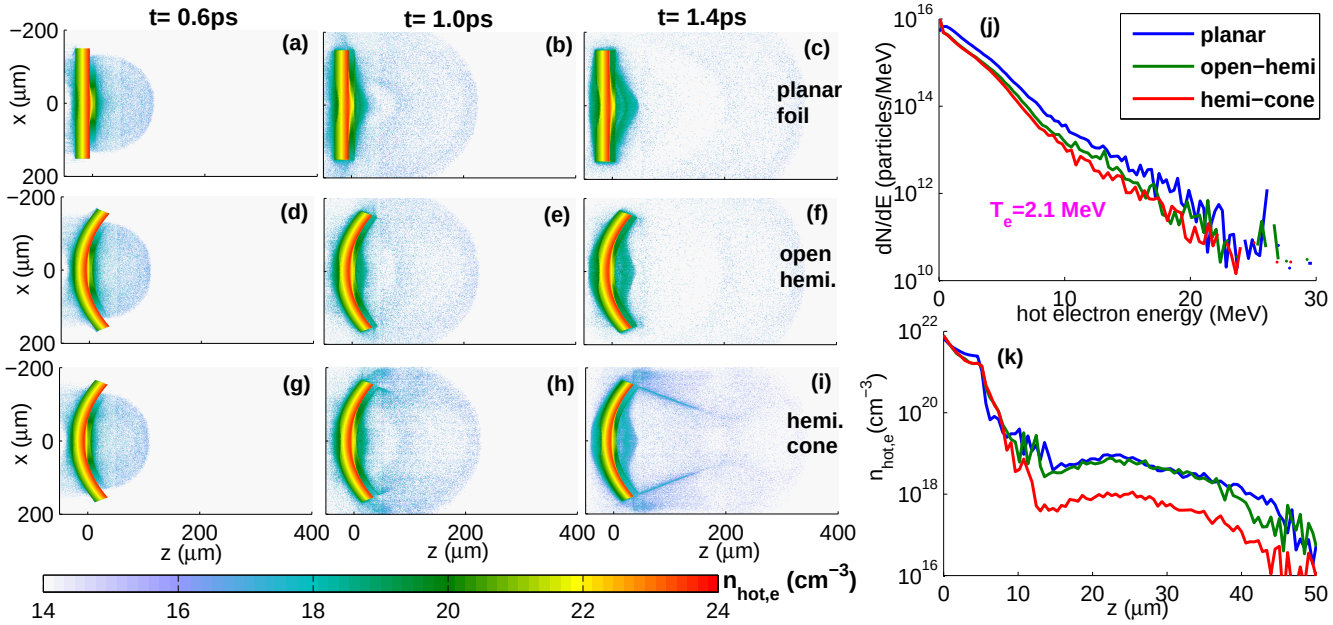

Figure 3 XXXXXXX 10Jan2013

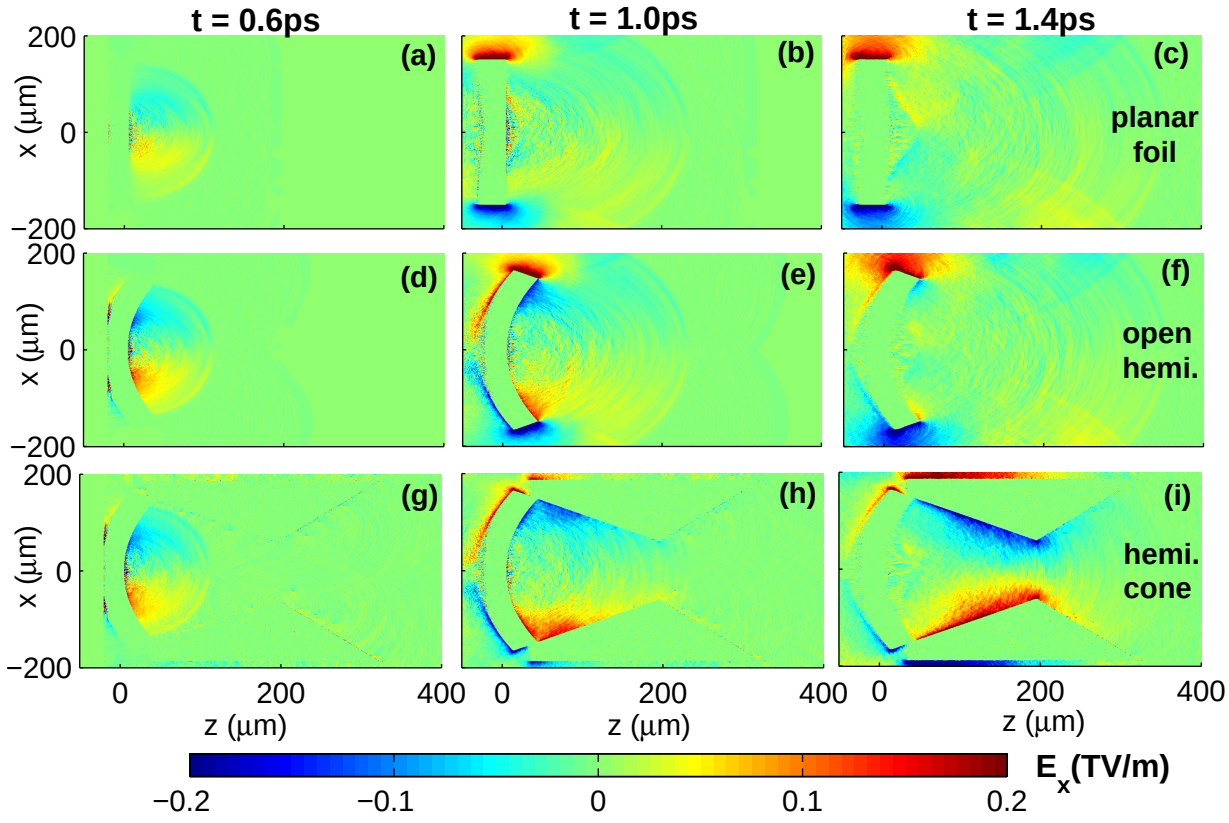

Figure 4 XXXXXXX 10Jan2013

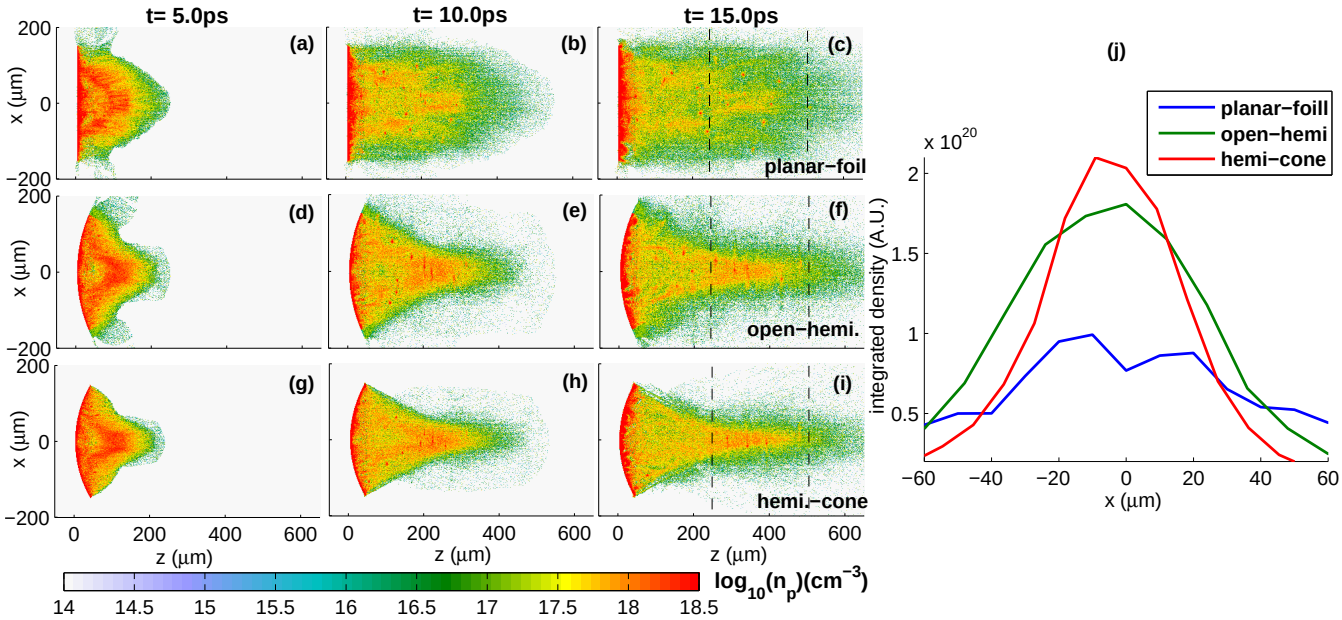

Figure 5 XXXXXXX 10Jan2013

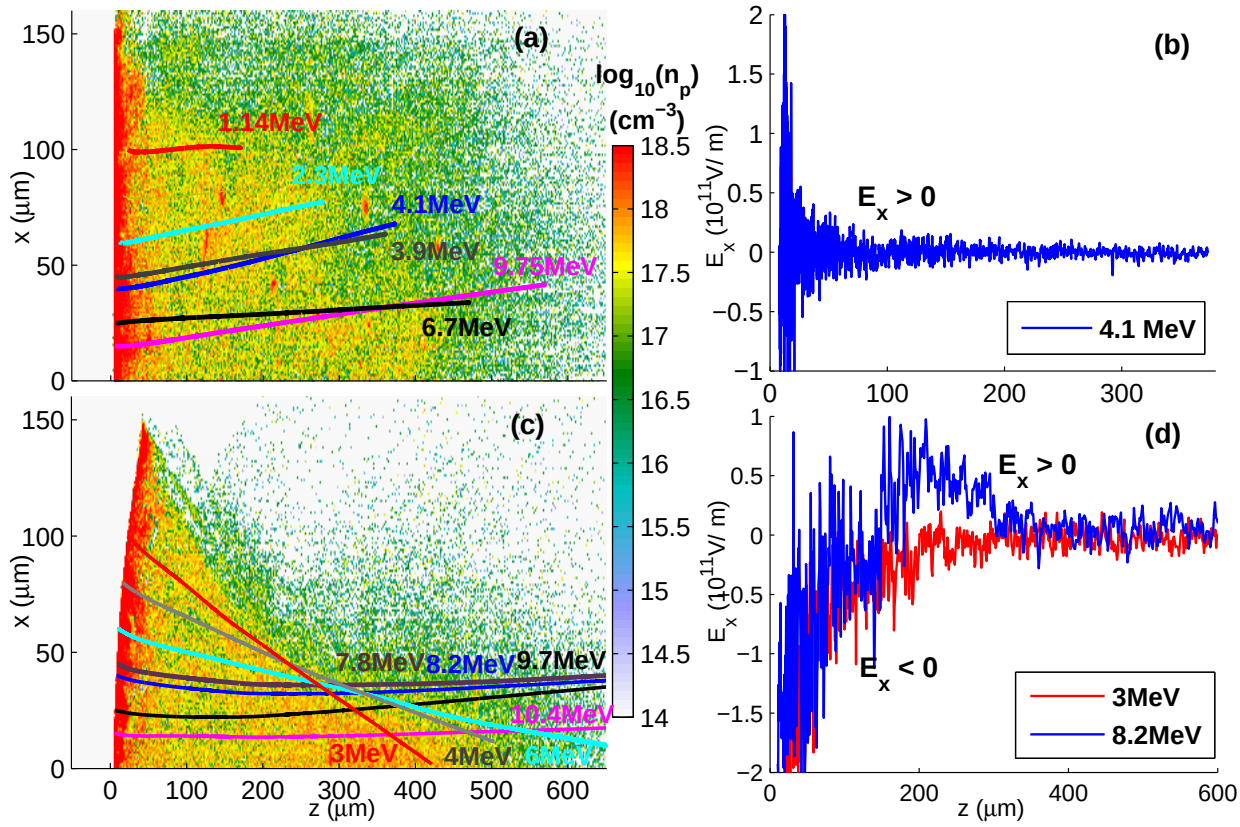

Figure 6 XXXXXXX 10Jan2013

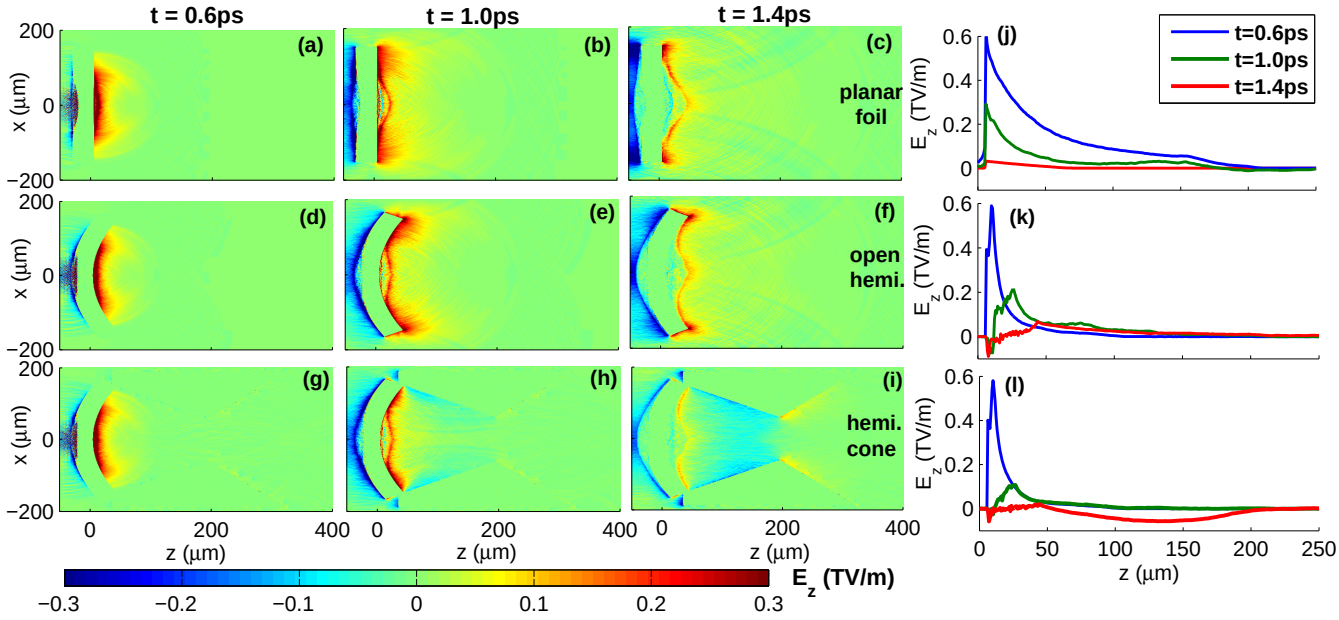

Figure 7 XXXXXXX 10Jan2013

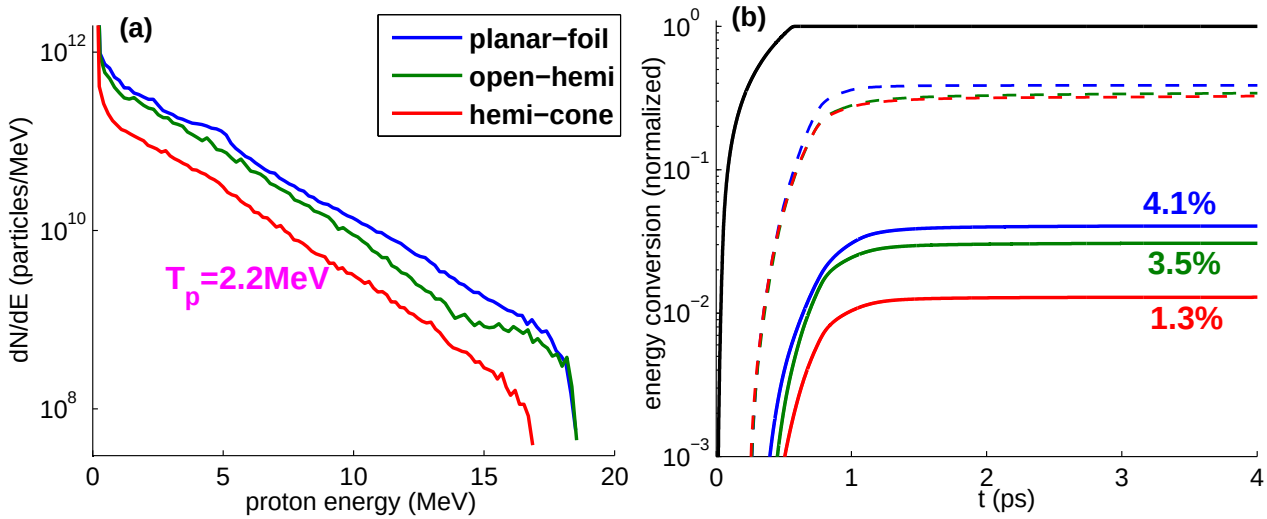

Figure 8 XXXXXXX 10Jan2013